Influence of a basal thermal anomaly on mantle convection

Nayuta Matsumoto [a], Atsuko Namiki [b,*], Ikuro Sumita [a]

[a] *Department of Earth Science, Kanazawa University, Kakuma, Kanazawa 920-1192, Japan*
[b] *University of California, Berkeley, Department of Earth & Planetary Science, 307 McCone Hall, Berkeley, CA 94720-4767, USA*

Abstract

We perform laboratory experiments to study the effects of a variable basal thermal anomaly on convection. In the regime of cellular convection ($Ra < 10^7$), the convection pattern changes as the horizontal temperature variation in the bottom boundary increases. When the temperature variation is less than the critical value, there is no effect to the convection pattern. Above this critical value, an upwelling is fixed at the site of the thermal anomaly. For a larger temperature variation, the upwelling region becomes wider. For the cases above the critical value, the time-averaged temperature in the isothermal core above the thermal anomaly becomes higher than that in the other regions. In the regime of plume dominant convection ($Ra \geq 10^7$), when the horizontal temperature variation exceeds the critical value, the location of a hot plume is similarly affected. For this case, the plume generated by the thermal anomaly straddles around the site of the thermal anomaly rather than being fixed. For a larger temperature variation, multiple plumes cluster together which also straddle around the anomaly. The straddling nature of the hot plumes generated by the thermal anomaly causes the time-averaged temperature above the thermal anomaly to remain unchanged. We also find that different from the cellular convection cases, the temperature variation less than critical is capable of generating intermittent hot plumes, but they do not dominate the convection pattern. The critical horizontal temperature variation needed to affect the convection pattern is found to be scaled by the maximum standard deviation of the time variation of the temperature σ^*_{max} around the lower thermal boundary layer in the absence of thermal anomaly. We estimate the possible temperature variation which can be generated by a partially molten region at the CMB. We find that assuming that σ^*_{max} for mantle is the same as that obtained from the experiment, a region less viscous than the surrounding region by an order of magnitude, can generate a hotspot.
© 2006 Elsevier B.V. All rights reserved.

Keywords: Mantle convection; Thermal anomaly; Plume; Hot spot; Partial melt

1. Introduction

During the last decade, seismic observations have revealed the presence of a strong lateral heterogeneity of seismic velocity at the core-mantle boundary region (Castle et al., 2000; Zhao, 2001; Tanaka, 2002) as well as

* Corresponding author. Tel.: +1 510 642 6331;
fax: +1 510 643 9980.
  E-mail address: namiki@eps.berkeley.edu (A. Namiki).
  URL: http://www.seismo.berkeley.edu/namiki/.

the presence of a ultra low velocity zone (ULVZ), latter of which is interpreted to be caused by partial melting (Williams and Garnero, 1996; Garnero, 2000; Lay et al., 2004).

If partial melting occurs at the base of the mantle, it might affect the heat transfer from the core to the mantle. This is because even only a few percent of partial melting yields huge viscosity reductions (Kohlstedt and Zimmerman, 1996), which in turn enhances the heat transfer. Distribution of ULVZ is not uniform (e.g., Garnero, 2000), suggesting that there might exist a lateral variation of melt fraction at the base of the mantle.

This could cause lateral heterogeneities of heat transfer from the core to the mantle which would then produce lateral temperature variations. Such localized region of anomalous heat flow at the site of ULVZ could generate hot plumes. On the other hand, a hot plume generated by the excess heat flux at the site of ULVZ would form a high temperature anomaly and can maintain the partially molten region. This positive feed back could sustain the long-lived hot plumes. Indeed, it has been argued that the geographical location of hot spots, which are considered to be the roots of hot plumes in the mantle, and low velocity regions at CMB and the ULVZ are correlated (Williams et al., 1998; Helmberger et al., 1998; Zhao, 2001; Burke and Torsvik, 2004; Thorne et al., 2004).

Under the assumption that hotspots are isolated thermal plumes in mantle convection (Morgan, 1971; Sleep, 1990; Duncan and Richards, 1991; Nataf, 2000), isolated plumes generated by localized heating in the absence of mean convection have been investigated (Griffiths and Campbell, 1990; Olson, 1990). However, the effect of the heterogeneous heating at the bottom of the vigorously convecting layer to the convection pattern has not been studied yet. In this study, we conduct a series of thermal convection experiments to study how the basal thermal anomaly affects the convection pattern. We classify the response of the convection pattern to the thermal anomaly as a function of magnitude of the thermal anomaly and Rayleigh number to infer the possible regime in the Earth's mantle.

2. Experimental method

The experimental apparatus is shown in Fig. 1. A cylindrical tank made of an acrylic plastic with an inner diameter of 260 mm and a thickness of 20 mm is used as a cell for thermal convection. The height of the convection cell is changeable and the upper and lower boundaries are made of aluminum plates with thicknesses of 18 and 5 mm, respectively. The upper plate is maintained at a constant temperature by circulating cold water from a temperature-controlled bath. The base plate is heated from below by a large annular silicone rubber film heater. In the center of the rubber film heater, a small ceramic square heater (10 mm × 10 mm) is attached to impose an anomalous heating. In the following, we call these heaters as "large" and "small" heater, respectively. A thermostat controlled AC power is supplied to the large heater to maintain a constant basal temperature at mid radius. A DC power is supplied to the small heater. Supplied wattage for both the large heater Q_l and small center heater Q_s are measured.
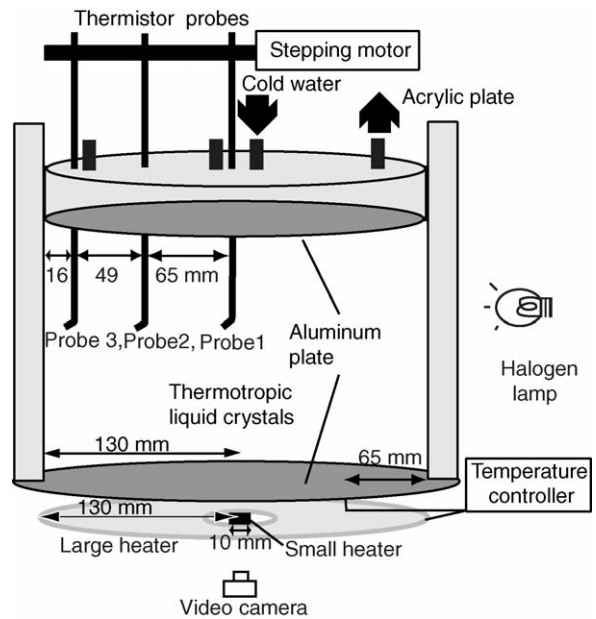

Fig. 1. A sketch of the experimental apparatus.

The actual magnitude of the thermal anomaly, in terms of wattage supplied to the fluid, is less than the ratio Q_s/Q_l, because the excess heat supplied by the small heater diffuses horizontally in the aluminum plate. As a result, the required wattage of the large heater needed to maintain the constant bottom temperature is reduced. The total wattage $Q_s + Q_l$, supplied to the fluid becomes approximately constant regardless of Q_s.

Three small thermistor probes (3.2 mm in length and 0.35 mm in diameter) are placed inside the cell at different radial distances from the center of the cylinder to measure the vertical temperature profile of the convecting fluid.

The probes are mounted on a stepping motor so that the local temperature of the fluid can be measured as a function of the distance away from the lower boundary with an accuracy of 0.01 mm. Each movable thermistor is calibrated with an accuracy of ±0.01 °C. The vertical temperature profiles are determined from the time-averaged measurements at each height. The number of measurement points in the vertical direction is 10–54.

The convection patterns are visualized by thermotropic liquid crystal powders which change the reflective color within the prescribed temperature range. A halogen light source passed through a slit is used to illuminate the fluids in vertical cross section, and the two-dimensional temperature fields of a three-dimensional convection are visualized. The temperature of the isothermal core of the convection layer is around

Table 1
Experimental conditions

Ra	Q_s (W)	Q_s fraction (%)	ΔT_h^*	Results	
2.5×10^5	0.0	0.0	0.029	No effect	Fig. 2N
2.5×10^5	0.3	0.6	0.044	No effect	
2.5×10^5	0.7	1.3	0.013	No effect	
2.5×10^5	1.3	2.5	0.048	No effect	
2.5×10^5	2.4	4.9	0.087	Effective	Fig. 2E
2.5×10^5	6.9	13.8	0.219	Effective	
2.5×10^5	13.0	26.1	0.366	Strongly effective	Fig. 2S
2.0×10^6	0.0	0.0	0.027	No effect	
2.0×10^6	0.2	0.5	0.046	No effect	
2.0×10^6	0.9	1.9	0.053	No effect	
2.0×10^6	2.0	4.3	0.095	Effective	
2.0×10^6	3.2	7.0	0.129	Effective	
2.0×10^6	5.8	12.8	0.186	Strongly effective	
2.0×10^6	7.6	16.8	0.248	Strongly effective	
1.0×10^7	0.0	0.0	0.017	No effect	Fig. 5N
1.0×10^7	0.2	0.5	0.053	Transient	Fig. 5T
1.0×10^7	0.6	1.4	0.055	Effective	
1.0×10^7	0.6	1.4	0.040	Transient	
1.0×10^7	1.1	2.6	0.048	Effective	Fig. 5E
1.0×10^7	2.0	4.7	0.078	Effective	
1.0×10^7	2.5	6.0	0.072	Strongly effective	
1.0×10^7	3.1	7.3	0.110	Strongly effective	
1.0×10^7	3.5	8.3	0.111	Strongly effective	Fig. 5S
1.0×10^7	3.9	9.2	0.137	Strongly effective	
1.0×10^7	4.5	10.7	0.154	Strongly effective	
1.0×10^7	4.9	11.5	0.132	Strongly effective	

Ra, Rayleigh number defined by Eq. (1); Q_s, heat supplied to the small heater; Q_s fraction, $Q_s/(Q_l + Q_s) \times 100$; ΔT_h^*, normalized horizontal temperature difference at the bottom of the convection layer, defined by Eq. (3).

25 °C and is close to the room temperature 23–26 °C. Estimated heat flux across the tank wall within the convecting region is less than 3% of the vertical heat flux. For a working fluid, we use 93 wt% glycerol solution with a Prandtl number, $Pr = \nu/\kappa > 10^3$, where ν is the kinematic viscosity and κ is the thermal diffusivity.

Experimental conditions and results are summarized in Table 1. Experiments are done at three Rayleigh numbers defined as,

$$Ra = \frac{g\alpha \Delta T_0 L^3}{\kappa \nu}, \tag{1}$$

where g is the gravitational acceleration, α the thermal expansion coefficient, ΔT_0 the temperature difference between bottom, T_b and top, T_t boundary temperatures, and L is the thickness of the convection layer. For the bottom temperature T_b, we use the temperature at mid radius of the cylindrical tank which is the thermostat controlled temperature of the large heater. The glycerol solution has a temperature dependent viscosity, and we use the approximate isothermal core temperature 25 °C to evaluate the viscosity. The viscosity variation in the

convection layer is less than a factor of 10. In the experiments, Rayleigh number is varied by changing the height of the convecting layer and the temperature difference across the layer.

Experiments are performed at $Ra = 2.5 \times 10^5$, 2.0×10^6 and 1.0×10^7, where the temperature differences are 21, 20 and 20 °C, the thicknesses of the convecting layer are 34, 64 and 108 mm, and the aspect ratios of the convection layer are 7.6, 4.1 and 2.4, respectively. The corresponding convection patterns for these Rayleigh numbers are classified as time-dependent three-dimensional flow, transient flow, and plume dominant convection, respectively (Krishnamurti, 1973; Manga and Weeraratne, 1999).

The experimental procedure is as follows. First, the upper and lower boundary temperatures are kept constant without heating by the small heater; i.e., $Q_s = 0$ W. We wait until the convection pattern attains a thermal equilibrium, which takes 4.5, 4.0 and 3.0 h for $Ra = 2.5 \times 10^5$, 2×10^6 and 10^7, respectively. After this time, we find that the measured temperature and heat flux also reached asymptotic values. Next, we turn on the small heater and
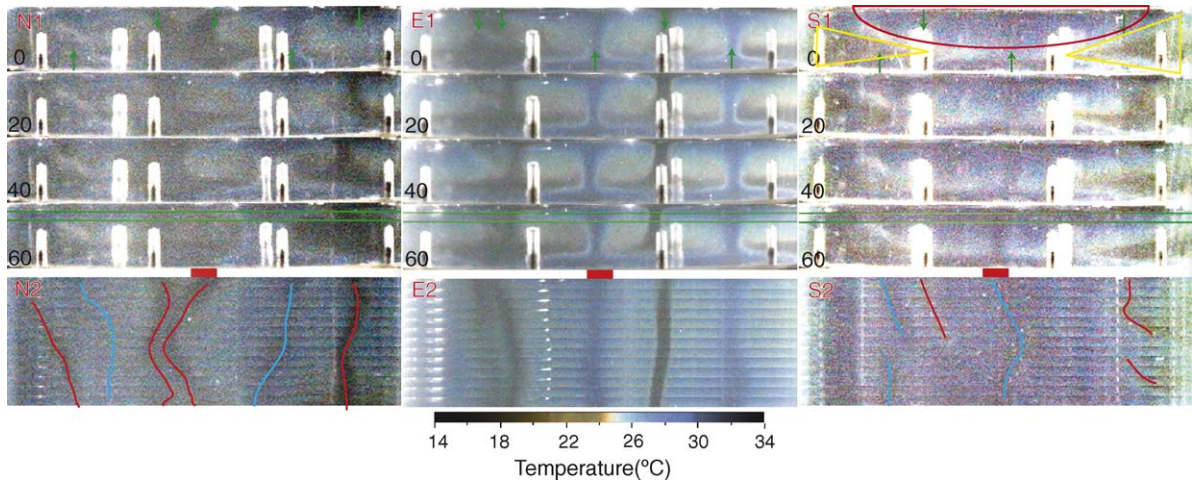
Fig. 2. (N1) Each panel shows the time evolution of the temperature field at 0, 20, 40 and 60 min after a thermal equilibrium was achieved. The horizontal and vertical dimensions are 160 and 34 mm, respectively. Red marker shows the location and width of the small heater. The Rayleigh number is $Ra = 2.5 \times 10^5$ and the anomalous heating of the small heater is $Q_s = 0$ W. Temperature field is visualized by thermotropic liquid crystals. A color bar indicates the temperature, where blue shows relatively hot regions (upwellings) and red to black shows cold regions (downwellings). The downwellings and upwellings are also indicated by green arrows. (N2) The time-evolution of the convective pattern in the height range indicated by two green lines in N1. Time increases towards the bottom in 5 min intervals and the total time span is 60 min. Red and blue lines indicate the sites of the downwellings and upwellings, respectively, which migrate horizontally with time. (E1 and E2) Results for $Q_s = 2.4$ W at same time intervals as N1 and N2. (S1 and S2) Results for $Q_s = 13$ W at same time intervals as N1 and N2. Red semicircle shows the region of warm fluid caused by anomalous heat flow. Yellow triangles show the region of concentrated downwelling flow towards the outer rim of the tank.

we further wait 5.0, 4.5 and 3.5 h for $Ra = 2.5 \times 10^5$, 2×10^6 and 10^7, respectively, and then start recording the convection pattern by a digital video camera. After that, we measure the temperature profile from bottom upwards. The time duration to calculate the time-averaged temperature for each height is 3 h, 45 min and 20 min for $Ra = 2.5 \times 10^5$, 2×10^6 and 10^7, respectively. These time scales are much longer than the growth time scales of the thermal boundary layers which is 2 min for the three Rayleigh numbers. Thermal diffusion time scale for the entire convection layer is 3.4, 11 and 34 h, respectively.

For each Rayleigh number, 7–12 experiments are done for different heating of the small heater Q_s.

3. Results

The basic states without the anomalous heating by the small heater are as follows. At $Ra = 2.5 \times 10^5$, convection cells are observed, whose location migrates horizontally as a function of time. At $Ra = 2 \times 10^6$, convection cells are still observed. However, cells deform its shape frequently from coalescence and separation. At $Ra = 10^7$, plumes which have heads and stems are observed and convection cells disappear.

From observing the convection pattern, we find that the response to the thermal anomaly differs for the case

where convection cells exist ($Ra = 2.5 \times 10^5$, 2×10^6) and the case where plumes are dominant ($Ra = 10^7$). We therefore describe these results separately in the following sections.

3.1. Effect of the thermal anomaly to convection cells

Three types of responses of the convection patterns are observed as the heating of the small heater Q_s is increased, which we classify as having "no effect", "effective" and "strongly effective". Fig. 2 shows the different responses of the convection patterns to the thermal anomaly at $Ra = 2.5 \times 10^5$ as Q_s is increased. Fig. 2N1 shows the convection patterns without the anomalous heating at the center ($Q_s = 0$ W) visualized by thermotropic liquid crystal powders. Blue correspond to hot regions and red to black correspond to cold regions. When there is no applied thermal anomaly, the upwelling and down-welling sites migrate horizontally as time elapses. The migration can be clearly recognized in Fig. 2N2. Similar convection patterns are observed for $Q_s = 0.3$, 0.7 and 1.3 W. We classify these patterns as "no effect".

For $Q_s = 2.4$ W, which corresponds to 4.9% of the total heat supply to the convection layer, an upwelling forms at the site of the small heater (Fig. 2E1), which does not migrate horizontally (Fig. 2E2). The typical aspect ratios
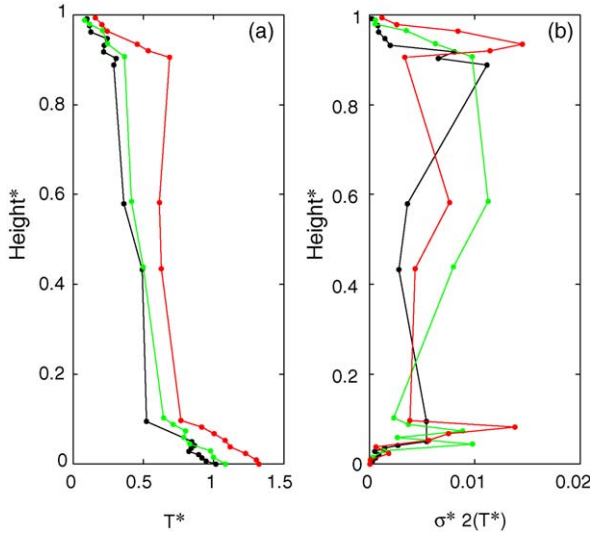
Fig. 3. (a) Time-averaged vertical temperature profiles for $Ra = 2.5 \times 10^5$ measured by probe 1 located above the small heater. Black, green and red lines indicate experiments with $Q_s = 0$, 2.4 and 13 W, respectively. T^* is the temperature normalized by the temperature difference across the convection layer, $T^* = (T - T_t)/\Delta T_0$. Height is scaled by the convection layer thickness. (b) Vertical profile of normalized variance $\sigma^{*2}(T^*)$ calculated from the temperature–time series data. The colors correspond to the same case shown in (a).

of the convection cells are the same as those observed in Fig. 2N1. We classify these patterns as "effective".

For $Q_s = 13$ W, which corresponds to 26% of the total heat supply to the convection layer, the aspect ratio of the convection cells at the site of the small heater becomes wider (see Fig. 2S2 at 40 min after thermal equilibrium was attained). The convection pattern resembles the horizontal convection which is driven only by the horizontal temperature difference (Rossby, 1965; Mori and Niino, 2002). The width of the hot region is wider than that of the small heater, and the location of the upwelling, which is the hottest region in the hot region, straddles around the site of the small heater (Fig. 2S2). We classify this convection pattern as "strongly effective".

The effect of the thermal anomaly is also apparent from the time-averaged vertical temperature profiles. Here we use a normalized temperature defined as

$$T^* = \frac{T - T_t}{\Delta T_0}. \tag{2}$$

Fig. 3a shows how the vertical temperature profile directly above the small heater changes as the heating of the small heater increases. The profile for the case $Q_s = 0$ W is shown by a black line, from which we can identify three layers from the bottom; the lower thermal boundary layer, a nearly isothermal layer representing the convecting region (isothermal core) and the upper

thermal boundary layer. For weak anomalous heating, the upper thermal boundary layer is less clearly defined compared to the lower boundary layer. As the anomalous heating increases, the basal temperature rises and the temperature gradient in the isothermal core becomes nearly zero. As a result, the upper thermal boundary layer becomes more distinct and the core temperature rises. This temperature profile is similar to those at higher Rayleigh numbers as shown in the following section. Here, the increase of the temperature at the boundary and the isothermal core alter the local Rayleigh number, because the temperature difference across the layer and the fluid viscosity are changed. Maximum increase of local Rayleigh number by anomalous heating is approximately twice the original value.

The vertical profile of the variance σ^{*2} calculated from the temperature–time series data also changes as Q_s increases. The black line in Fig. 3b shows the case without the anomalous heating ($Q_s = 0$ W). This profile does not show noticeable peaks. On the other hand, when the anomalous heating increases, peaks of variances appear at the normalized heights of 0.1 and 0.95 which are around the borders of the thermal boundary layers and the isothermal core. This type of variance profile is also usually observed at higher Rayleigh numbers. Note the variance at mid depth is strongly affected by the lateral migration of convection cells whose behavior is chaotic. We thus discuss the profile only at around the thermal boundary layer.

By comparing the temperature measurements using the three probes at different radial distances from the small heater, we can study the horizontal effect of the anomalous heating. For no anomalous heating ($Q_s = 0$ W), although the core temperatures vary horizontally, the temperature gradient within the thermal boundary layers at the three sites are similar (Fig. 4a). The corresponding variance profiles at three sites also do not show noticeable peaks (Fig. 4b).

For an anomalous heating of $Q_s = 13$ W, we find that the temperature profiles measured above the small heater are different from those at other locations. The temperature gradients within the upper and lower thermal boundaries above the small heater are larger than those at other sites, indicating horizontal variation of heat flux (Fig. 4c). The temperatures and their gradients of the isothermal core also vary horizontally. Above the small heater, both peaks of variance at the top and bottom of the convecting layer are observed (Fig. 4d). The profile at mid-radius of the convection tank shows only the upper peak, and the profile at outermost radius shows only the lower peak. This result can be interpreted to be caused by the accumulation of a warm fluid beneath
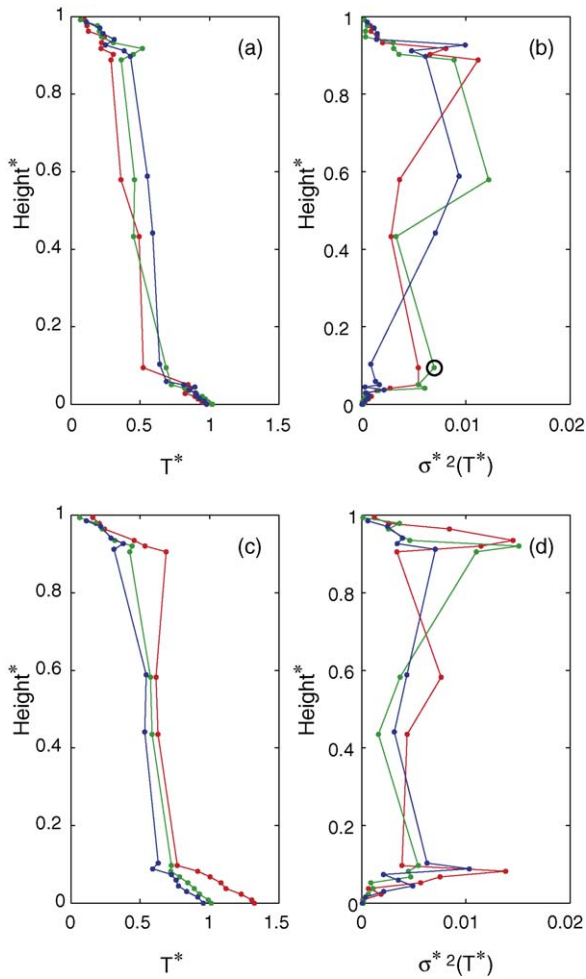
Fig. 4. (a) Vertical temperature profiles for $Ra = 2.5 \times 10^5$. Results for $Q_s = 0$ W. Red, green and blue lines are the profiles for the probes 1–3, respectively, whose positions are indicated in Fig. 1. (b) Vertical profile of variance σ^{*2} for (a). Black circle indicates the value used for $\sigma_{max}^{*2}(Q_s = 0)$. (c and d) Results for $Q_s = 13$ W. The lines correspond to same probes shown in (a and b).

the upper boundary above the site of the small heater, which spreads to the mid radius. In contrast, the downwelling flow is concentrated near the outer rim of the tank. This interpretation is consistent with the visual observation of Fig. 2S1. The hot blue region indicated by a red line is located above the site of a small heater, and is surrounded by yellow cold region indicated by yellow triangles.

Similar results are also obtained from the experiments at $Ra = 2 \times 10^6$. As the anomalous heating increases, the location of an upwelling becomes fixed and the convection cell becomes wider. When the thermal anomaly affects the convection, the temperature of the isothermal core above the thermal anomaly also increases.

3.2. Effect of the thermal anomaly to plumes

In the case of $Ra = 10^7$, the regime of plume dominant convection, four types of responses are observed which we classified as "no effect", "transient", "effective" and "strongly effective".

Fig. 5N1 shows the convection patterns without the anomalous heating ($Q_s = 0$ W). Here, plumes with distinct heads and stems are observed. Hot plumes rise intermittently and their roots are not fixed. Fig. 5N2 shows the random nature of the location of the hot plumes.

Fig. 5T2 shows the experiment for $Q_s = 0.2$ W, which corresponds to 0.5% of the total heat supply. In this case, hot plumes rise from the site above the small heater more frequently than the case without the anomalous heating ($Q_s = 0$ W). The hot plumes rise intermittently and most of the hot plumes do not reach the top boundary (Fig. 5T1). Although the effects of the thermal anomaly are apparent, they do not dominate the convection pattern so we define this response as "transient".

For $Q_s = 1.1$ W, which corresponds to 2.6% of the total heat supply to the convection layer, a narrow hot plume rises from the left side of the small heater (Fig. 5E1) and straddles around the site of the small heater (Fig. 5E2). The plume rises continuously and reach the top of the convection layer so we define this response as "effective".

For $Q = 3.5$ W, which corresponds to 8.3% of the total heat supply, a cluster of hot plumes are observed around the site of the small heater (Fig. 5S1). They occasionally coalesce to form a wider hot plume. The location of a plume or a cluster of plumes straddle around the site of the small heater (Fig. 5S2). We define this pattern as "strongly effective".

We next consider the vertical temperature profile. Compared to the case for $Ra = 2.5 \times 10^5$, the effect of the thermal anomaly is not apparent. The temperature and temperature gradient of the isothermal core is unchanged despite the anomalous heating (Fig. 6a). This is one of the major differences between the case with convection cells and the case with plumes. In the case of convective cells, the thermal anomaly makes a persistent upwelling above it and the time averaged temperature of the isothermal core becomes larger. However, when the thermal anomaly makes hot plumes, the hot plumes straddle around the thermal anomaly and as a result, the time-averaged temperature of the isothermal core hardly changes. On the other hand, the temperature gradients within the thermal boundary layers become larger as the anomalous heating increases, indicating the enhancement of the heat flux.
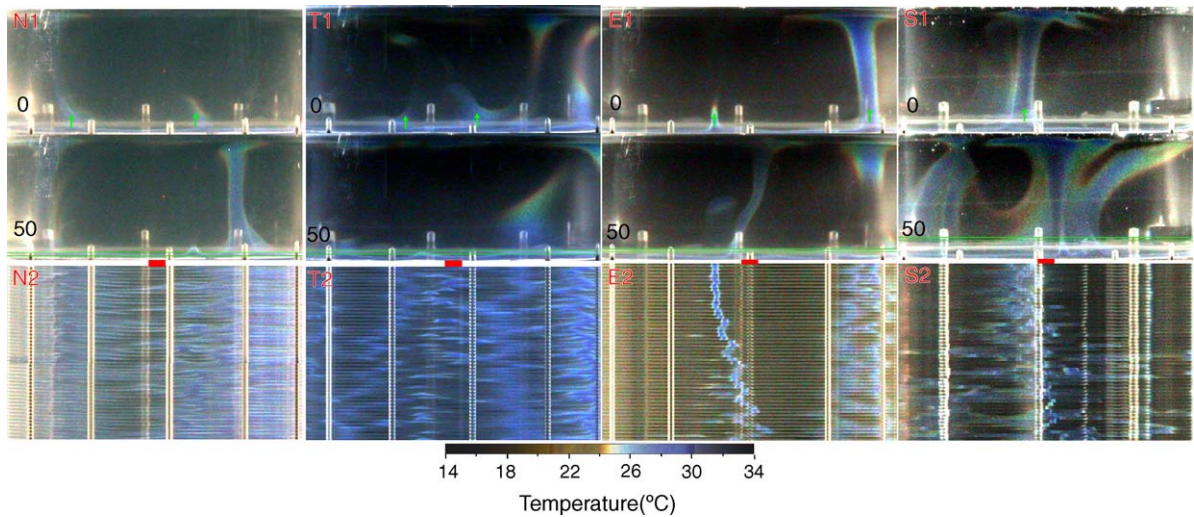
Fig. 5. (N1) Temperature field for $Ra = 10^7$. Two panels show the time evolution of the temperature field 0 and 50 min after the thermal equilibrium is attained. The horizontal and vertical dimensions are 190 and 108 mm, respectively. Red marker shows the location and width of the small heater. (N2) The time-evolution of the convective pattern in the band shown by two green lines in N1. Time increases toward the bottom in 1 min intervals and the total time span is 50 min. (T1 and T2) Results for $Q_s = 0.2$ W at same time intervals as N1 and N2. (E1 and E2) Results for $Q_s = 1.1$ W at same time intervals as N1 and N2. (S1 and S2) Results for $Q_s = 3.5$ W at same time intervals as N1 and N2.

The black line in Fig. 6b shows the vertical profile of variance σ^{*2} for $Q_s = 0$ W. We can identify two peaks around a normalized height of 0.05 and 0.95 which are at the borders of the isothermal core and the thermal boundary layer. When the anomalous heating is increased, a third peak of variance appears beneath the upper peak around the normalized height of 0.85. We interpret this peak as the consequence of warm fluid that rises from the small heater and accumulates beneath the upper ther-
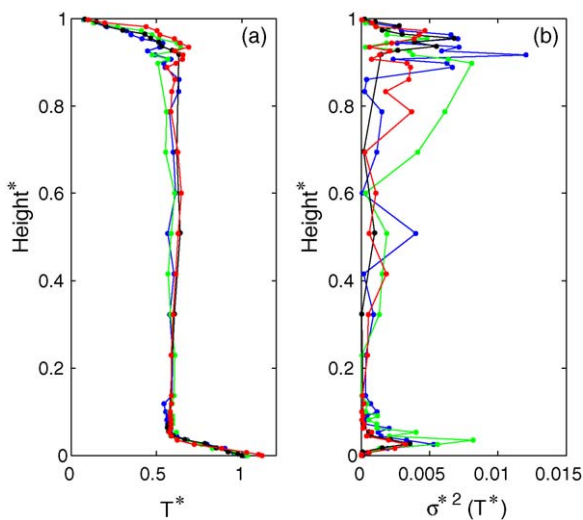

Fig. 6. (a and b) Vertical profile of time-averaged temperature and its variance for $Ra = 10^7$. Black, blue, green and red lines indicate experiments with $Q_s = 0$, 0.2, 1.1 and 4.9 W, respectively.

mal boundary layer. When cold plumes traverse across this layer, it causes a large temperature fluctuation. When the anomalous heating is increased further, this peak decreases again. This suggests that the traverse of cold plumes is prevented by the excess supply of warm fluid.

Fig. 7 shows the horizontal effect of the anomalous heating. For $Q_s = 0$ W, the temperature and variance profiles are horizontally similar (Fig. 7a and b). Different from the low Rayleigh number cases, there are no horizontal variations of the time-averaged isothermal core temperature for both cases, $Q_s = 0$ and 4.9 W (Fig. 7a and c). For the case of $Q_s = 4.9$ W, the temperature gradients within the thermal boundary layers above the small heater are larger than those of others, indicating that the heat flux varies horizontally.

The variance profile shows that the profile measured using two inner probes are similar; i.e., both have the third peak of the variance beneath the upper thermal boundary layer (Fig. 7d). This suggests that the excessively supplied warm fluid extend horizontally as far as to this radius. On the other hand, the profile for the outermost probe shows another peak of variance above the lower peak, suggesting the cold fluid accumulates at this radius. The variance of upper boundary is larger than that for lower boundary. This can be attributed to the effect of the temperature dependent viscosity; i.e., temperature dependent viscosity makes the temperature difference in the upper thermal boundary layer larger than that of the lower thermal boundary.
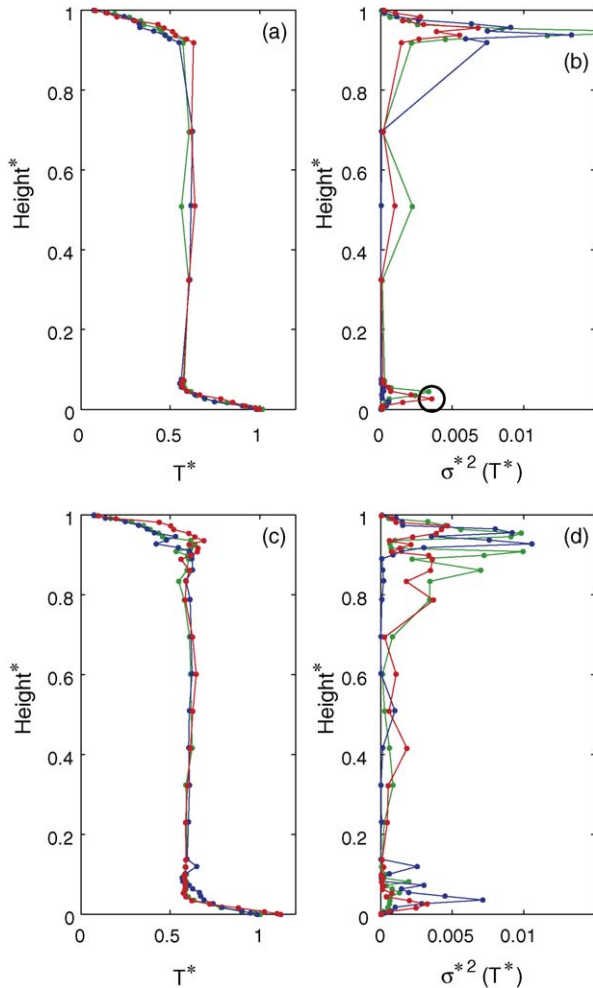
Fig. 7. (a and b) Vertical profile of average temperature and its variance for $Ra = 10^7$ and $Q_s = 0$ W. The lines correspond to same probes shown in Fig. 4. (c and d) Same as (a and b) but for $Q_s = 4.9$ W.

4. Discussion

Our experiments show that anomalous heating can affect convection patterns and that the response to the thermal anomaly differs between the case with cellular convection and the case with plume dominant convection. In the following, we derive the criteria which determine the pattern of convection.

4.1. Threshold to affect convection

As previously noted, an accurate evaluation of heat flux anomaly is difficult in our apparatus. We therefore use the horizontal temperature variation at the bottom of the fluid, rather than the heat flux anomaly, as a measure of the imposed thermal anomaly. We define

the normalized horizontal temperature anomaly ΔT_h^* as

$$\Delta T_h^* = \frac{T_1 - T_3}{\Delta T_0} \tag{3}$$

where subscripts 1 and 3 indicate the temperature measurements at probe 1 (above the small heater) and 3 (the outer most) at the bottom boundary. Thus, $T_1 - T_3$ is a measure of the maximum horizontal temperature variation.

We propose that if the imposed temperature variation at the bottom boundary exceeds the temperature fluctuations in the fluid resulting from convection, the convection patterns would be altered. This is because the convection alone cannot sufficiently homogenize the anomalously heated fluid parcel. As an estimate of the temperature fluctuation in the fluid, we take the maximum standard deviation of temperature fluctuations near the lower thermal boundary layer, σ_{max}^*, in the absence of anomalous heating ($Q_s = 0$ W) for each Rayleigh number as indicated in Figs. 4b and 7b. In Fig. 8, we plot the convective regimes as a function of Rayleigh number and a non-dimensional parameter which measures the magnitude of the thermal anomaly

$$\gamma = \frac{\Delta T_h^*}{\sigma_{max}^*(Q_s = 0)}. \tag{4}$$

From Fig. 8, we find that $\gamma = 1$ approximately forms the threshold for the imposed thermal anomaly to affect the convection pattern. For $Ra < 10^7$ where convection cells are observed, $\gamma \simeq 1$ separates the regimes "no effect" and "effective". For $Ra \geq 10^7$, plume dominate convection, $\gamma \simeq 1$ approximately separates the regimes "transient" and "effective".

These results indicate that for $\gamma \geq 1$, the thermal anomaly affects the convection patterns regardless of the magnitude of the Rayleigh number of the mean convection. For $\gamma < 1$, the effect of thermal anomaly depends on whether convection has cells or plumes. When plumes dominate convection pattern, plumes detach after they rise, and the boundary layer becomes homogenized. In this case, a weak thermal anomaly ($\gamma < 1$) is sufficient to generate a hot plume, although it does not dominate the convection. This is observed as "transient" regime. However, for cellular convection, the up- and downwellings never detach from the lower and upper thermal boundaries so the boundary layer does not become homogenized. In this case, a weak thermal anomaly ($\gamma < 1$) is insufficient to shift these up- and downwellings.
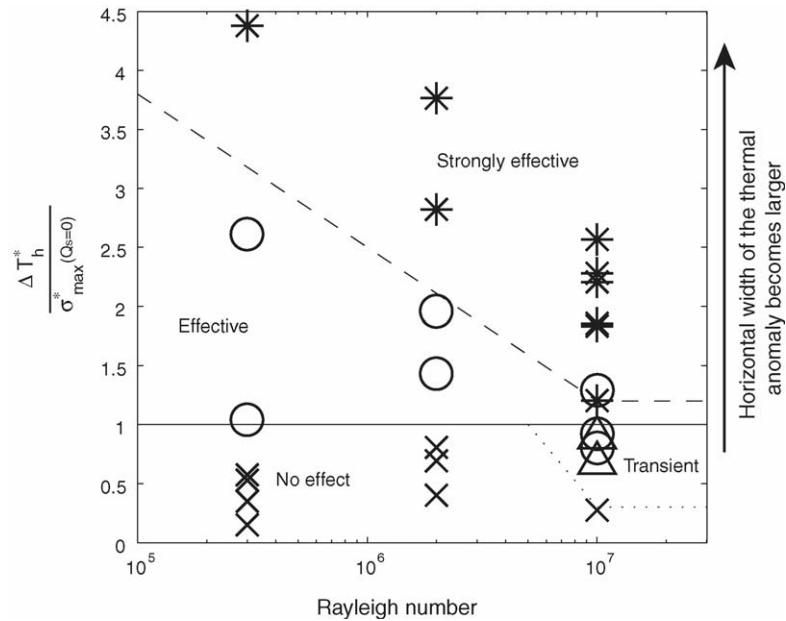
Fig. 8. Regime diagram of the responses of the convection patterns to the thermal anomaly as a function of Rayleigh number and the magnitude of the imposed thermal anomaly. The magnitude of the thermal anomaly is defined by Eq. (4) as $\gamma = \Delta T_h^* / \sigma_{max}^* (Q_s = 0)$ where ΔT_h^* is the non-dimensional horizontal temperature variation at the bottom. $\sigma_{max}^* (Q_s = 0)$ is the non-dimensional maximum temperature fluctuations near the lower thermal boundary in the absence of anomalous heating, and are $\sigma_{max}^* (Q_s = 0) = 0.084, 0.066$ and 0.060 for $Ra = 2.5 \times 10^5, 2 \times 10^6$ and 1.0×10^7, respectively. Cross, triangle, circle, and asterisk indicate convection patterns which we are classified as having no effect, a transient effect, effective and strongly effective, respectively.

4.2. Threshold to affect convection strongly

We next consider the regime boundary between the "effective" and "strongly effective" regimes. In the case of "strongly effective" the up welling above the thermal anomaly becomes wider and several hot plumes form a cluster. We infer that the transition from "effective" to "strongly effective" occurs when the horizontal width of the thermal anomaly exceeds the width of the convection cell or the horizontal spacing of the plumes. To accommodate this thermal anomaly, the aspect ratio of the convection cell and plume spacing must change, and the convection pattern becomes strongly modified.

In Fig. 8, the threshold for "strongly effective" appears at larger γ than that for "effective". This is consistent with the mechanism discussed above. In our experiments, a larger γ proportional to $T_1 - T_3$ yields a larger width of the thermal anomaly by thermal diffusion in the bottom aluminum plate.

Here, we also infer that the critical width to yield "strongly effective" convection depends inversely on Rayleigh number from the negative slope of the threshold for "strongly effective" in Fig. 8. This is because the aspect ratio of the convection cells or the ratio of

plume spacing to the thickness of the convection layer becomes smaller for higher Rayleigh number as shown in our visual observations. The fact that the regime of "effective" is very narrow for $Ra = 10^7$ in Fig. 8 is also explained by the same reasoning. The horizontal scale of the small heater is comparable to the average spacing of the plumes in the absence of the thermal anomaly. Therefore, a small increase of the width of the thermal anomaly by thermal diffusion is capable of exceeding the average spacing between the plumes, causing them to cluster.

4.3. Locations of plumes

Here, we consider the unsteady nature of the plumes observed in the "effective" and "strongly effective" cases, where the root of the hot plume generated by the anomalous heating straddles around the location of the heater (Figs. 2 and 5). There are two possible explanations for this behavior. First, the radius of the thermal anomaly may be larger than the size of the small heater due to thermal diffusion in the bottom plate. Second, the most gravitationally unstable region may not be directly above the highest temperature region, but above the region with largest horizontal tempera-
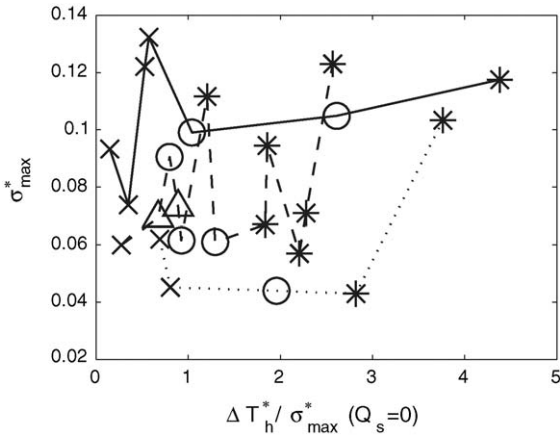
Fig. 9. The measured maximum standard deviation around the lower thermal boundary layer at the site of the small heater as a function of the magnitude of the thermal anomaly defined by Eq. (4). Solid, dotted and dashed lines indicate $Ra = 2.5 \times 10^5$, 2.0×10^6 and 10^7, respectively. Marks correspond to those used in Fig. 8.

ture gradient (Mori and Niino, 2002). The region with the largest horizontal temperature gradient will then appear as an annulus around the small heater such that the hot plumes would straddle above the annulus. Conversely, if the diameter of the annulus around the thermal anomaly is smaller than the plume width, we infer that the thermal anomaly would fix the root of the plume just above it without any straddling behavior. In our experiments, the width of the small heater, which is the minimum width of the thermal anomaly, is larger than the width of a plume, and such fixation is not observed at $Ra \geq 10^7$.

4.4. Effect to the standard deviation of temperature fluctuations

When a hot plume is fixed by a thermal anomaly, time variation of temperature at a given place is reduced. This could be observable as a change of standard deviations of temperature variation. We plotted the normalized maximum standard deviation of the time variation of the temperature σ^*_{max} around the lower thermal boundary layer at the site of the small heater as a function of the magnitude of the thermal anomaly γ defined by Eq. (4) in Fig. 9. This figure does not show systematic correlation between σ^*_{max} and the observed convection patterns, although we were able to discuss some relation between the vertical profile of σ^{*2}_{max} and convection patterns in Figs. 3, 4, 6 and 7. This fact suggests that it is difficult to infer the convection pattern only from a representative standard deviation σ^*_{max}.

5. Implications to the Earth's mantle

5.1. Theoretical estimate of lateral temperature difference

Assuming that ULVZ is a partially molten region, seismically observed heterogeneous distribution of ULVZ (Garnero, 2000; Thorne and Garnero, 2004) suggests that a lateral variation of melt fraction exists in the lower most mantle. Such laterally heterogeneous distribution of the partial melt can cause a laterally heterogeneous heat transfer from the core to the mantle, and could maintain the anomalous temperature distribution at the lower most mantle. In this section, we estimate the possible magnitude of the thermal anomaly supplied by ULVZ to discuss whether this positive feedback works to fix the loci of hot plumes in the mantle.

It is reasonable to assume a thermo-chemical boundary layer as suggested by Lay et al. (2004) and assumed in theoretical (Sleep, 1988), numerical (Hansen and Yuen, 1988; Farnetani, 1997; Tackley, 1998; Montague and Kellogg, 2000; McNamara and Zhong, 2004; Nakagawa and Tackley, 2004), and experimental studies (Olson and Kincaid, 1991; Davaille, 1999a; Davaille et al., 2002; Jellinek and Manga, 2002). This is because strongly temperature dependent viscosity of mantle rock may cause small scale convection in this region (Solomatov and Moresi, 2002) and chemical heterogeneities can result from subducted slabs and chemical reaction between the mantle and core (Hofmann and White, 1982; Knittle and Jeanloz, 1991; Kellogg and King, 1993; Christensen and Hofmann, 1994; van der Hilst et al., 1997). We regard that the thickness of the chemically dense layer is the same or thinner than that of the D'' layer. This is because the complicated features which suggest the existence of chemical heterogeneity are found within the D'' layer. Such feature cannot be fully explained by the recently discovered post-perovskite phase transition (e.g., Hirose et al., 2006).

We thus assume the structure of the lower most mantle as shown in Fig. 10a. As shown in this figure, we assume that there is a localized region with partial melt (dark grey area) surrounded by a region without partial melt (light grey area). For simplicity we assume that in the region with partial melt, the melt fraction in the entire depth range of the chemically dense layer is uniform. In this situation, we regard that both the regions with and without partial melt convect. This is because the estimated Rayleigh number for the chemically dense layer whose thickness is 120 km, a typical thickness of the D'' layer, exceeds the critical Rayleigh number for the onset the convection ($Ra_c \sim 700$), if its viscosity is 10^{21} Pa s and a
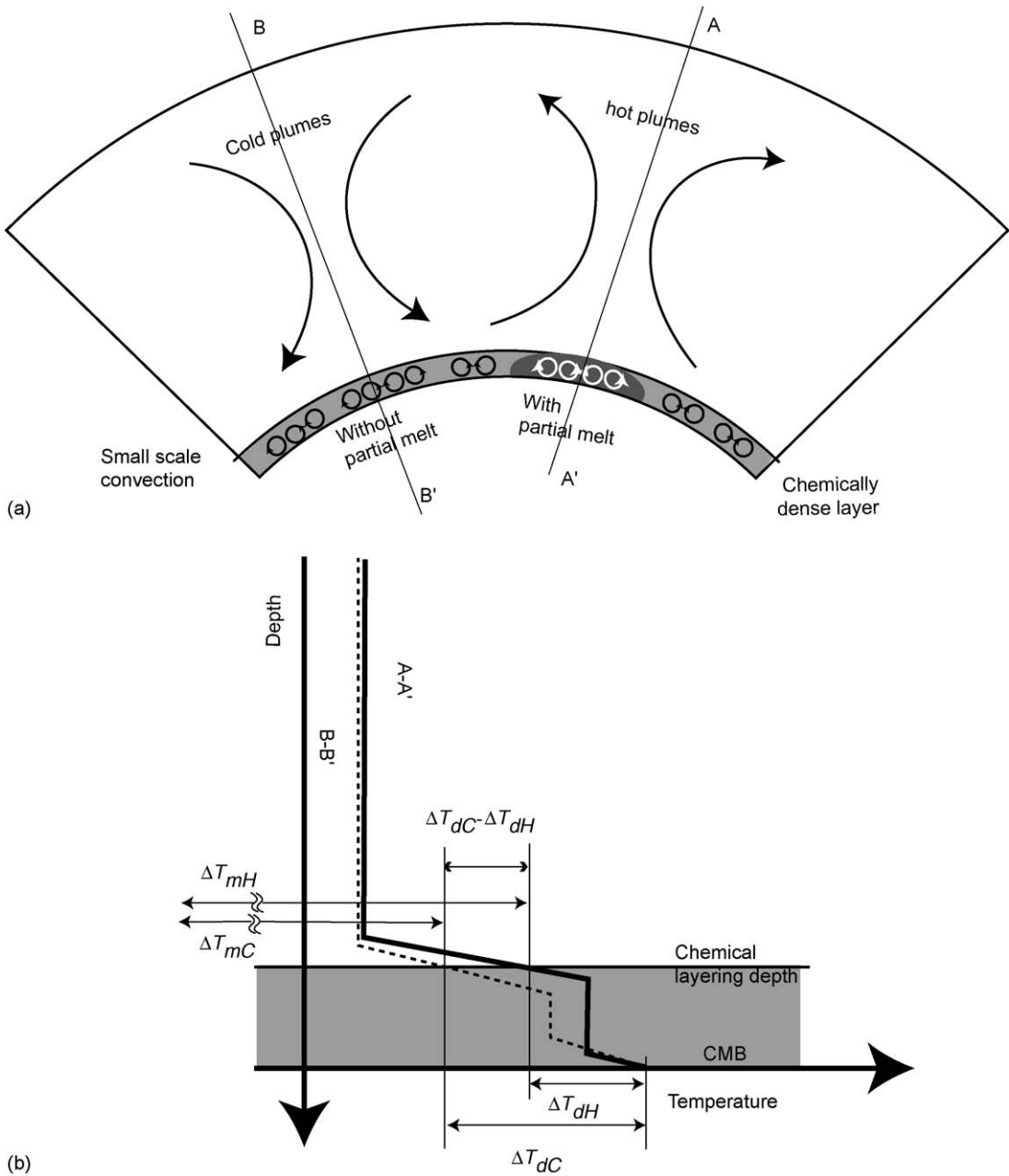
Fig. 10. (a) A schematic diagram showing the regions with and without partial melt in the chemically dense layer. (b) Corresponding temperature profiles for (a). Solid and dotted lines correspond to A-A′ and B-B′ sections, respectively.

vertical temperature difference is 500 °C (e.g., Schubert et al. (2001)). A viscosity of 10^{21} Pa s is a typical viscosity for mantle and the viscosity for the chemically dense layer will be smaller than this value because of its temperature dependent viscosity. These facts suggest that a chemically dense layer with a thickness less than 120 km can convect.

In what follows, we estimate the lateral temperature variation between the region with and without partial melt at the interface between mantle and the chemically dense layer. First, we estimate the appropriate temperature profiles at vertical cross sections A-A′ and B-B′. When small scale convection develops in the chemically dense layer, we can model the mantle convection as

a two-layered convection. Assuming that heat is transferred only in the radial direction, from the heat balance between the mantle and chemically dense layers, we obtain the following relation (Namiki and Kurita, 2003)

$$k_{\mathrm{m}} \frac{\Delta T_{\mathrm{m}}}{\delta_{\mathrm{m}}} = k_{\mathrm{d}} \frac{\Delta T_{\mathrm{d}}}{\delta_{\mathrm{d}}}. \tag{5}$$

where subscripts m and d indicate mantle and chemically dense layers, k the thermal conductivity, and δ is the thickness of the thermal boundary layer,

$$\delta \propto \frac{L}{Ra^{1/3}}. \tag{6}$$

Rayleigh number Ra is defined by Eq. (1), so Eq. (5) includes physical properties of k, ρ, α, κ, and viscosity η. Among these parameters, only viscosity can vary by an order of magnitude in the CMB region, and the effect of other physical properties to the heat transfer is limited. We thus assume that physical parameters other than η are similar between upper and lower layers. Eq. (5) can then be rewritten as

$$\frac{\Delta T_{\mathrm{m}}^4}{\eta_{\mathrm{m}}} = \frac{\Delta T_{\mathrm{d}}^4}{\eta_{\mathrm{d}}}. \tag{7}$$

From Eq. (7), we find that a locally low viscous chemically dense layer has a smaller radial temperature difference. In this estimate, we neglect the effect of the entrainment. The mass flux to the other layer by entrainment is restricted unless the density difference between the upper and lower layer is very small and difficult to affect the vertical temperature profile (Davaille, 1999b; Gonnermann et al., 2002; Namiki, 2003).

We can estimate the possible viscosity contrast between the chemically dense layer and the lower mantle as follows. When the temperature is subsolidus, we can use an Arrhenius type viscosity function

$$\eta = \eta^{\star} \exp \left\{ \frac{E}{R} \left(\frac{1}{T} - \frac{1}{T^{\star}} \right) \right\} \tag{8}$$

where E is the activation energy, R the gas constant, $T^{\star}$ the reference mantle temperature and $\eta^{\star}$ is the reference viscosity. Assuming $E = 500$ kJ/mol (Yamazaki and Karato, 2001), $T^{\star} = 2500$ K, and mean temperature for the chemically dense layer as 3500 K (Boehler, 2000), the average viscosity contrast becomes about $\eta_{\mathrm{d}}/\eta_{\mathrm{m}} \sim 10^{-3}$. Considering Eq. (7), this viscosity ratio imply $\Delta T_{\mathrm{m}} > \Delta T_{\mathrm{d}}$.

We can apply this relationship for the regions with partial melt (A-A′) and region without partial melt (B-B′) in Fig. 10a,

$$\frac{\Delta T_{\mathrm{mH}}^4}{\eta_{\mathrm{mH}}} = \frac{\Delta T_{\mathrm{dH}}^4}{\eta_{\mathrm{dH}}} \tag{9}$$

$$\frac{\Delta T_{\mathrm{mC}}^4}{\eta_{\mathrm{mC}}} = \frac{\Delta T_{\mathrm{dC}}^4}{\eta_{\mathrm{dC}}}, \tag{10}$$

where subscripts H and C indicate the regions with and without partial melt which would be hot and cold regions, respectively. Here, as we previously showed, $\Delta T_{\mathrm{m}} > \Delta T_{\mathrm{d}}$ and $\eta_{\mathrm{m}} \gg \eta_{\mathrm{d}}$. In addition, Fig. 7c shows that lateral temperature variation of the isothermal core in the convecting layer is insignificant at high Rayleigh number convection, even if the layer has a effective thermal anomaly at its bottom. We thus neglect the distinction between these two regions in the mantle, i.e., $\Delta T_{\mathrm{m}} \sim \Delta T_{\mathrm{mH}} \sim \Delta T_{\mathrm{mC}}$ and $\eta_{\mathrm{m}} \sim \eta_{\mathrm{mH}} \sim \eta_{\mathrm{mC}}$. The normalized lateral temperature difference at the interface of the mantle and the chemically dense layer then becomes

$$\frac{\Delta T_{\mathrm{dC}} - \Delta T_{\mathrm{dH}}}{\Delta T_{\mathrm{m}}} \frac{\eta_{\mathrm{dC}}^{1/4} - \eta_{\mathrm{dH}}^{1/4}}{\eta_{\mathrm{m}}^{1/4}}. \tag{11}$$

These equations indicate that if the viscosity of the chemically dense layer of the region with partial melt is smaller than that of the region without partial melt, $\eta_{\mathrm{dH}} < \eta_{\mathrm{dC}}$, then the radial temperature difference across the dark gray region in Fig. 10a becomes smaller than that in the light gray region; i.e., $\Delta T_{\mathrm{dH}} < \Delta T_{\mathrm{dC}}$, as shown in Fig. 10b. This generates the lateral temperature variation $\Delta T_{\mathrm{dC}} - \Delta T_{\mathrm{dH}}$ at the interface of the mantle and chemically dense layer. Low viscosity regions caused by partial melts can thus generate high temperature anomalies at the bottom of the mantle convection. The lateral temperature variation becomes larger as the viscosity contrast between these two regions becomes larger.

It is well known that even a few percent of partial melt allows huge viscosity reductions (Kohlstedt and Zimmerman, 1996). Assuming that the mean temperature for these two regions of the chemically dense layer is comparable but partial melt further reduces the viscosity by a factor of 1/10, the viscosity contrast between the partially molten chemically dense layer and the mantle above becomes $\eta_{\mathrm{dH}}/\eta_{\mathrm{m}} \sim 10^{-4}$. The normalized lateral temperature anomaly then becomes $\Delta T_{\mathrm{h}}^* = (\Delta T_{\mathrm{dC}} - \Delta T_{\mathrm{dH}})/\Delta T_{\mathrm{m}} \sim 0.078$.

For a larger degree of partial melting, even larger viscosity reduction is possible which leads to a larger lateral temperature variation. The temperature in the dense layer beneath the cold plumes should be colder than the average temperature 3500 K used in this estimate. If convection does not occur in the region without partial melt of the chemically dense layer because of its high viscosity, the efficiency of heat transfer is reduced, and this leads to a larger lateral temperature variation. Thus, $\Delta T_{\mathrm{h}}^* \sim 0.078$ is a minimum estimate.

5.2. Influence of the thermal anomaly to the hotspots locations

In order to apply the estimated magnitude of lateral thermal anomaly ΔT_{h}^* to the Earth's mantle, we need to know the standard deviation of the temperature fluctuations in the mantle convection, $\sigma_{\max}^*(Q_{\mathrm{s}} = 0)$. Assuming that $\sigma_{\max}^*(Q_{\mathrm{s}} = 0)$ of the mantle is similar to the thermal convection in our experiments, we can apply the experimentally derived condition $\sigma_{\max}^*(Q_{\mathrm{s}} = 0) = 0.060$ to the mantle, using the appropriate Rayleigh number for mantle convection 10^7.

In this case, the minimum estimate of lateral temperature anomaly in the mantle, $\Delta T_{\mathrm{h}}^* \sim 0.078$, exceeds the critical value to affect the convection pattern, $\sigma_{\max}^*(Q_{\mathrm{s}} = 0) = 0.060$, indicating that partial melt at the CMB region can generate a hot plume.

We remark however that our experiments lack many of the complicated features of mantle convection, and that the value of $\sigma_{\max}^*(Q_{\mathrm{s}} = 0)$ for mantle convection could become different from the experimental value. For example, the presence of strongly temperature dependent viscosity and internal heating in the mantle convection could make the temperature fluctuations around the bottom boundary smaller than that near the upper boundary. This would cause the mantle convection to become more sensitive to the basal thermal anomaly. On the other hand, it is uncertain how the subducted slab affect $\sigma_{\max}^*(Q_{\mathrm{s}} = 0)$.

From our experiments, we infer that if a thermal anomaly whose magnitude exceeds the critical $\gamma > 1$, "effective" or "strongly effective" convection patterns would appear in mantle convection. As we discussed in the previous section, we infer that whether convection pattern become "effective" or "strongly effective" type depends on the lateral extent of the thermal anomaly. If this criteria can be directly applied to the mantle, the transition from "effective" to "strongly effective" type of convection would depend on the lateral extent of partially molten region.

Seismological studies have shown that the lateral width of the ULVZ and very low shear wave velocity region has a large variation. Recent seismological observation have revealed a partially molten region with a small width at the east of Australia, $\sim 50 \, \mathrm{km}$ (Rost et al., 2005). This width is comparable to that of the plume width estimated from the thermal boundary layer thickness (Namiki and Kurita, 1999). Such a small thermal anomaly might fix an isolated hotspot. If the width of the thermal anomaly is larger than the width of a plume but smaller than the spacing of the plumes, our experiments suggest that an hot spot would straddle around the thermal anomaly. If the width of the thermal anomaly is larger than the width of the spacing of plumes, plumes would cluster. A very low shear wave velocity region with a width as large as 500 km has been found beneath the South Pacific super plume (Tanaka, 2002). This might be an outcome of the "strongly effective" regime in the mantle; i.e., laterally large thermal anomaly makes a plume cluster which may be observed as a super plume because of the limited resolution of seismological observations (Schubert et al., 2004).

When the width of the thermal anomaly is larger than the width of the plume, the plume straddles around the thermal anomaly. The migration velocity of each plume straddling in the restricted area should be slower than that without the thermal anomaly, so this might be observed as a relative slow motion. When a plume straddles, the plume would prefer to be located at the annulus around the thermal anomaly because this is where the largest lateral temperature gradient exists and is gravitationally most unstable. The geographic distribution of the shear wave velocity anomaly and the location of hot spots show that hot spots which originated from CMB tend to be located more likely above the regions of largest lateral gradients of shear wave velocity than above the low velocity regions (Courtillot et al., 2003; Ritsema and Allen, 2003; Burke and Torsvik, 2004; Thorne et al., 2004). This may be the consequence of such straddling nature of the plumes.

6. Conclusion

On the basis of our experiments we conclude that when the magnitude of the basal thermal anomaly is sufficiently large, a hot plume is generated above it. The threshold to generate a hot plume is defined by γ, the ratio of basal temperature anomaly to the standard deviation of the time variation of temperature around the lower thermal boundary layer. We estimated thermal anomaly generated by partial melt at CMB region, and find that it can exceed the experimentally obtained threshold, suggesting a thermal coupling between ULVZ and hot spots.

References

Boehler, R., 2000. High-pressure experiments and the phase diagram of lower mantle and core materials. Rev. Geophys. 38, 221–246.

Burke, K., Torsvik, T.H., 2004. Derivation of large igneous provinces of the past 200 million years from long-term heterogeneities in the deep mantle. Earth Planet. Sci. Lett. 227, 531–538.

Castle, J.C., Creager, K.C., Winchester, J.P., van der Hilst, R.D., 2000. Shear wave speeds at the base of the mantle. J. Geophys. Res. 105, 21543–21557.

Christensen, U.R., Hofmann, A.W., 1994. Segregation of subducted oceanic-crust in the convecting mantle. J. Geophys. Res. 99, 19867–19884.

Courtillot, V., Davaille, A., Besse, J., Stock, J., 2003. Three distinct types of hotspots in the Earth's mantle. Earth Planet. Sci. Lett. 205, 295–308.

Davaille, A., 1999a. Simultaneous generation of hotspots and super-swells by convection in a heterogeneous planetary mantle. Nature 402, 756–760.

Davaille, A., 1999b. Two-layer thermal convection in miscible viscous fluids. J. Fluid Mech. 379, 223–253.

Davaille, A., Girard, F., LeBars, M., 2002. How to anchor hotspots in a convecting mantle? Earth Planet. Sci. Lett. 203, 621–634.

Duncan, R.A., Richards, M.A., 1991. Hotspots, mantle plumes, flood basalts, and true polar wander. Rev. Geophys. 29, 31–50.

Farnetani, C.G., 1997. Excess temperature of mantle plumes: The role of chemical stratification across D''. Geophys. Res. Lett. 24, 1583–1586.

Garnero, E.J., 2000. Heterogeneity of the lowermost mantle. Ann. Rev. Earth Planet. Sci. 28, 509–537.

Gonnermann, H.M., Manga, M., Jellinek, A.M., 2002. Dynamics and longevity of an initially stratified mantle. Geophys. Res. Lett. 29, 1399, doi:10.1029/2002GL014851.

Griffiths, R.W., Campbell, I.H., 1990. Stirring and structure in mantle starting plumes. Earth Planet. Sci. Lett. 99, 66–78.

Hansen, U., Yuen, D.A., 1988. Numerical simulations of thermal–chemical instabilities at the core-mantle boundary. Nature 334, 237–240.

Helmberger, D.V., Wen, L., Ding, X., 1998. Seismic evidence that the source of the iceland hotspot lies at the core-mantle boundary. Nature 396, 251–255.

Hirose, K., Karato, S., Cormier, V.F., Brodholt, J.P., Yuen, D.A., 2006. Unsolved problems in the lowermost mantle. Geophys. Res. Lett. 33, L12S01, doi:10.1029/2006GL025691.

Hofmann, A.W., White, W.M., 1982. Mantle plumes from ancient oceanic crust. Earth Planet. Sci. Lett. 57, 421–436.

Jellinek, A.M., Manga, M., 2002. The influence of a chemical boundary layer on the fixity, spacing and lifetime of mantle plumes. Nature 418, 760–763.

Kellogg, L.H., King, S.D., 1993. Effect of mantle plumes on the growth of D'' by reaction between the core and mantle. Geophys. Res. Lett. 20, 379–382.

Knittle, E., Jeanloz, R., 1991. Earth's core-mantle boundary: results of experiments at high pressures and temperatures. Science 251, 1438–1443.

Kohlstedt, D.L., Zimmerman, M.E., 1996. Rheology of partially molten mantle rocks. Annu. Rev. Earth Planet. Sci. 24, 41–62.

Krishnamurti, R., 1973. Some further studies on the transition to turbulent convection. J. Fluid Mech. 60, 285–303.

Lay, T., Garnero, E.J., Williams, Q., 2004. Partial melting in a thermochemical boundary layer at the base of the mantle. Phys. Earth Planet. Int. 146, 441–467.

Manga, M., Weeraratne, D., 1999. Experimental study of non-boussinesq Rayleigh-Benard convection at high Rayleigh and Prandtl numbers. Phys. Fluids 11, 2969–2979.

McNamara, A.K., Zhong, S., 2004. The influence of thermochemical convection on the fixity of mantle plumes. Earth Planet. Sci. Lett. 222, 485–500.

Montague, N.L., Kellogg, L.H., 2000. Numerical models of a dense layer at the base of the mantle and implications for the geodynamics of D''. J. Geophys. Res. 105, 11101–11114.

Morgan, W.J., 1971. Convection plumes in the lower mantle. Nature 230, 42.

Mori, A., Niino, H., 2002. Time evolution of nonlinear horizontal convection: its flow regimes and self-similar solutions. J. Atmos. Sci. 59, 1841–1856.

Nakagawa, T., Tackley, P.J., 2004. Thermo-chemical structure in the mantle arising from a three-component convective system and implications for geochemistry. Phys. Earth Planet. Int. 146, 125–138.

Namiki, A., 2003. Can the mantle entrain D''? J. Geophys. Res. 108, 2487, doi:10.1029/2002JB002315.

Namiki, A., Kurita, K., 1999. The influence of boundary heterogeneity in experimental models of mantle convection. Geophys. Res. Lett. 26, 1929–1932.

Namiki, A., Kurita, K., 2003. Heat transfer and interfacial temperature of two-layered convection: implications for the D''-mantle coupling. Geophys. Res. Lett. 30, 1023, doi:10.1029/2002GL015809.

Nataf, H.-C., 2000. Seismic imaging of mantle plumes. Annu. Rev. Earth Planet. Sci. 28, 391–417.

Olson, P., 1990. Hot spots, swells and mantle plumes. In: Ryan, M.P. (Ed.), Magma transport and storage. John Wiley & Sons Ltd., pp. 33–51.

Olson, P., Kincaid, C., 1991. Experiments on the interaction of thermal convection and compositional layering at the base of the mantle. J. Geophys. Res. 96, 4347–4354.

Ritsema, J., Allen, R.M., 2003. The elusive mantle plume. Earth Planet. Sci. Lett. 207, 1–12.

Rossby, H.T., 1965. On thermal convection driven by non-uniform heating from below: an experimental study. Deep Sea Res. 12, 9–16.

Rost, S., Garnero, E.J., Williams, Q., Manga, M., 2005. Seismological constraints on a possible plume root at the core-mantle boundary. Nature 435, 666–669.

Schubert, G., Masters, G., Olson, P., Tackley, P., 2004. Superplumes or plume clusters? Phys. Earth Planet. Int. 146, 147–162.

Schubert, G., Turcotte, D.L., Olson, P., 2001. Mantle Convection in the Earth and Planets. Cambridge University Press, Cambridge.

Sleep, N.H., 1988. Gradual entrainment of a chemical layer at the base of the mantle by overlying convection. Geophys. J. 95, 437–447.

Sleep, N.H., 1990. Hotspots and mantle plumes: some phenomenology. J. Geophys. Res. 95, 6715–6736.

Solomatov, V.S., Moresi, L.-N., 2002. Small-scale convection in the D'' layer. J. Geophys. Res. 107, 2016, doi:10.1029/2000JB000063.

Tackley, P.J., 1998. Three-dimensional simulations of mantle convection with a thermo-chemical basal boundary layer: D''? In: Gurnis, M., Wysession, M.E., Knittle, E., Buffett, B.A. (Eds.), The Core-mantle Boundary Region. AGU, Washington, DC, pp. 231–253.

Tanaka, S., 2002. Very low shear wave velocity at the base of the mantle under the south Pacific superswell. Earth Planet. Sci. Lett. 203, 879–893.

Thorne, M.S., Garnero, E.J., 2004. Inferences on ultralow-velocity zone structure from a global analysis of SPdKS waves. J. Geophys. Res. 109, B08301, doi:10.1029/2004JB003010.

Thorne, M.S., Garnero, E.J., Grand, S.P., 2004. Geographic correlation between hot spots and deep mantle lateral shear-wave velocity gradients. Phys. Earth Planet. Inter. 146, 47–63.

van der Hilst, R.D., Widiyantoro, S., Engdahl, E.R., 1997. Evidence for deep mantle circulation from global tomography. Nature 386, 578–584.

Williams, Q., Garnero, E.J., 1996. Seismic evidence for partial melt at the base of Earth's mantle. Science 273, 1528–1530.

Williams, Q., Revenaugh, J., Garnero, E., 1998. A correlation between ultra-low basal velocities in the mantle and hot spots. Science 281, 546–549.

Yamazaki, D., Karato, S., 2001. Some mineral physics constrains on the rheology and geothermal structure of Earth's lower mantle. Am. Mineral. 86, 385–391.

Zhao, D., 2001. Seismic structure and origin of hotspots and mantle plumes. Earth Planet. Sci. Lett. 192, 251–265.